Available online at www.sciencedirect.com

ScienceDirect

journal homepage: www.elsevier.com/locate/he

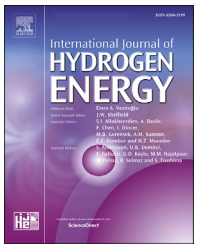

Microstructural and electrochemical properties of Ni-impregnated GDC10 and 8YSZ freeze tape cast scaffolds as fuel electrodes for solid oxide cells

Davide Cademartori [a,*], *Davide Clematis* [a], *Maria Paola Carpanese* [a,b]

[a] *Department of Civil, Chemical and Environmental Engineering, University of Genoa (UNIGE-DICCA), Via all'Opera Pia 15, 16145 Genoa, Italy*

[b] *Institute of Condensed Matter Chemistry and Technologies for Energy, National Research Council (CNR-ICMATE), c/o DICCA-UNIGE, Italy*

HIGHLIGHTS

- The electrode design optimization is expected to increase its electrochemical performance.
- Nanostructured graded porous electrodes for SOCs are shaped combining freeze tape casting and infiltration.
- The anisotropy of gas diffusion channels is highlighted by the 3D reconstruction of the GDC10 scaffold.
- The Ni-infiltrated GDC10 freeze tape cast scaffold is measured to be the best performing electrode architecture.
- The electrochemical performance of the Ni-GDC10 electrode is mainly hindered by its low electronic conductivity.

ARTICLE INFO

Article history:
Received 9 July 2023
Received in revised form
26 September 2023
Accepted 3 October 2023
Available online 19 October 2023

Keywords:
Solid oxide cells
Freeze tape casting
Infiltration
Electrochemical impedance spectroscopy
X-ray tomography

ABSTRACT

Ni-impregnated $Gd_{0.1}Ce_{0.9}O_2$ and $Y_{0.08}Zr_{0.92}O_2$ fuel electrodes for solid oxide cells are manufactured by the combination of the freeze tape casting and infiltration techniques. Their morphological properties are investigated by scanning electron microscope and X-Ray microtomography while their electrochemical performance is evaluated in symmetrical $Y_{0.08}Zr_{0.92}O_2$-supported button cells by electrochemical impedance spectroscopy. The microstructural analysis of the manufactured scaffolds highlights the characteristic anisotropy of porosity provided by the freeze tape casting method. The average tortuosity factor across the out of plane direction has been calculated equal to 1.38, being considerably lower than the average values of the other components, ($\tau_x = 10.2$) and ($\tau_y = 6.87$). The contribution provided by gas diffusion to the overall polarization resistance of the freeze tape cast electrodes has been estimated around $6{\cdot}10^{-4}$ Ω cm^2 in the 600–750 °C temperature range, thus lower than the best reported values for the state-of-the-art electrodes featuring sponge-like porosity. The measured impedance data highlighted the higher electrochemical performance of the Ni-impregnated $Gd_{0.1}Ce_{0.9}O_2$ architecture, holding a polarization resistance of 0.823 Ω cm^2 at 750 °C, which is regarded as a very promising result for a ~600 μm thick electrode. The interpretation of the impedance data was supported by the distribution of relaxation times analysis and the complex non-linear least square fit. In particular, the electrochemical investigation highlighted the presence of two major resistive contributions which have been ascribed to the occurrence of a chemical capacitance within the GDC10 lattice (low frequency contribution) and to the multi-layered

* *Corresponding author.*
E-mail address: davide.cademartori@edu.unige.it (D. Cademartori).

https://doi.org/10.1016/j.ijhydene.2023.10.027

architecture of the tested symmetrical cells which increases the contact losses (high frequency contribution).

1. Introduction

Solid Oxide Cells (SOCs) are energy conversion devices able to produce electrical power when operating in fuel cell (SOFC) mode or convert electrical energy into chemicals when working in electrolysis (SOEC) mode. They are expected to play a key role in an energy scenario grounded on the widespread use of renewable sources, finding applications in industrial sectors dealing with grid balancing, seasonal energy storage and production of synthetic e-fuels thanks to the advantages provided by their operating reversibility, fuel flexibility (they can indeed be supplied with H_2, NH_3 and hydrocarbon-based compounds) and conversion efficiency [1,2].

The state-of-the-art SOCs operate at high temperature (at least 700 °C) and consist of multiple ceramics layers featuring porous electrodes sandwiching a thin dense electrolyte. Conventional SOCs materials are Ni-yttria-stabilized zirconia (YSZ) for the fuel electrode, YSZ for the electrolyte and doped ceria-lanthanum strontium cobalt ferrite (LSCF) for the air electrode [3–5].

SOCs operate thanks to electrochemical reactions taking place in the active sites of the electrodes (triple phase boundary, TPB, sites) where gas, electron-conducting and ionic-conducting phases meet and carry out the fuel and oxygen electro-oxidation/reduction. In conventional SOCs architectures, a functional layer featuring a fine porous structure is usually added at the interface between the electrolyte and the fuel electrode to increase the density of TPB (λ_{TPB}) and enhance the number of electrochemical reaction sites [6,7]. The starting ceramic suspensions of conventional shaping routes, such as tape casting and screen printing [8,9], use functional raw powders showing a particle size distribution (PSD) in the 0.5–50 μm range, with finer particle size employed for the active layer. However, in Ni-YSZ cermets, some of the degradation phenomena have been ascribed to the inherent materials characteristics while others (Ni migration and coarsening) were directly attributed to the electrodes microstructural properties and, specifically, to the PSD of the solid phases [10,11]. Due to the electrochemical performance limitations and degradation phenomena observed when employing μm-PSD, increased attention has been progressively posed to the development of nanostructured electrodes [12–16]. Specifically, a smaller electrocatalyst particle size shows enhanced electrochemical activity due to its higher specific surface area. Nanostructured electrodes have been reported to show significantly higher electrochemical performance, inhibit Ni coarsening and reduce the degradation rate during operation [17–20]. The infiltration (or impregnation) technique is regarded as the main manufacturing route to fabricate nanostructured fuel electrodes. It holds the advantages of being a simple integration process, low cost and does not require high-temperature sintering, which is needed for traditional fuel electrode integration. In the impregnation process, a liquid precursor solution containing the stoichiometric amount of metal salts, is usually introduced into a porous scaffold and heat treated to decompose the salts and generate the desired functional material [21]. Multiple infiltration cycles are usually necessary to add the desired amount of impregnated phase and decorate the backbone walls.

A large electrode activity towards redox reactions must also be accompanied by cells microstructural properties which promote high electrochemical performance, chemical and structural stability over time. In particular, the amount and distribution of porosity play a key role in the diffusion of gases through the electrodes, thus affecting both the mass transfer and reactions rate. In conventional fabrication methods for SOCs electrodes such as tape casting, screen printing, extrusion and dip coating [8,9,22], porosity is generated by the addition to the starting ceramic suspensions of pore-forming agents which are subsequently burnt out during the sintering process [8,23–25]. The final porosity, derived from organic pore formers such as starch or graphite, results to be randomly distributed throughout the bulk matrix of the electrodes, generating tortuous gas diffusion channels also including isolated pores not being interconnected [26,27]. Gas diffusion limitations in both fuel and air electrodes of SOFCs and SOECs have widely been reported in literature [28–30] and contribute to the increase of degradation rate during operation. The need for improvement both in cell performance and stability over time can be fulfilled by the adoption of tailored electrodes microstructures which enable rapid gas turnover within the diffusion channels and lower the concentration polarization resistance. Therefore, microstructural optimization and low-cost substrates preparation are regarded as the promising key directions for the development of the next generation of SOCs [31].

Within this context, the freeze tape casting method can provide ceramic structures with unique morphological properties including hierarchical and directional porosity [32–35]. The operating principle of water-based freeze tape casting holds many similarities with the conventional tape casting manufacturing technique where a ceramic suspension, featuring ceramic powders and additives (solvent, dispersant, binder, plasticizers, etc.) is deposited over a film-carrier. However, in the preparation of the initial ceramic suspension to be freeze tape cast no organic pore-formers are included because, after the casting step, the green tape is frozen at low operating temperature (−10–45 °C) and then

dried to remove the ice crystals and shape a porous layered membrane [36,37].

Therefore, the major advantage of freeze tape casting is represented by the opportunity of enabling the anisotropic growth of the solvent crystals when the tape is frozen over a cold source. The unidirectional thermal gradient, which is established along the tape thickness, shapes graded crystals which grow towards the air exposed surface and, after removal by sublimation, leave room to directional hierarchical porosity. Freeze tape cast electrode architectures have been reported to improve the electrochemical performance of SOCs thanks to the enhancement of gas diffusion [38–40] which is also expected to reduce the degradation rate over time.

With the purpose of developing an innovative electrode architecture for SOCs, able to boost gas diffusion and reduce activation losses, this work focuses on the morphological and electrochemical characterization of Ni-impregnated graded porous backbones of 10% gadolinia doped ceria (GDC10) and 8% Yttria stabilized zirconia (8YSZ) as fuel electrodes for SOCs. Specifically, ion conducting scaffolds of GDC10 and 8YSZ are firstly shaped by freeze tape casting and secondly infiltrated with a precursor solution of Ni nitrate for the in-situ generation of electrocatalyst nanoparticles. The morphology of the diffusion layer is characterized by Scanning Electron Microscope (SEM) micrographs and 3D reconstructions obtained from X-ray micro-tomography. In particular, the tortuosity factor, average dimension of pores and phases volume fractions are extracted to evaluate the gas diffusion resistance of the graded porous electrode microstructure. The electrochemical characterization of nanostructured freeze tape cast scaffolds of GDC10 and 8YSZ is then carried out by electrochemical impedance spectroscopy (EIS). The EIS data of the impregnated electrodes are also compared to those measured on a pure freeze tape cast GDC10 scaffold to evaluate the impact of the Ni nanoparticles on the electrochemical performance. Eventually, an in-depth focus on the electrochemical properties of the Ni-GDC10 architecture is carried out with the support of equivalent circuit (EC) modelling and the distribution of relaxation times (DRT) analysis. The investigation of the EIS data as function of the operating temperature and H_2 partial pressure enables the deconvolution of the electrochemical steps limiting the performance of the electrode.

2. Materials and methods

2.1. Experimental manufacturing process

The procedure for the manufacturing of a freeze tape cast backbone follows the same operating steps reported in our previous work focusing on the shaping of hierarchical supports of GDC10 and 8YSZ [40]. A starting water-based suspension to be freeze tape cast was prepared using as received GDC10 (TREIBACHER, Austria) and 8YSZ (TZ-8Y, Tosoh Corporation) and adding an acrylic latex emulsion as water insoluble binder to avoid any interference between the additives and the water crystallization process. The composition of the GDC10 and 8YSZ-based starting suspension is reported in Table 1.

The initial suspension was ball milled for 24 h using spherical zirconia milling media and subsequently transferred for 4 h into a glass beaker, where low speed mixing (100 rpm) was operated by a magnetic stirrer. The first stage included water, dispersant and ceramic powders while binder, arabic gum and Surfynol SE-F were added after the ball milling process. Before casting, the suspensions were deaired under vacuum for 3–5 min to deplete the entrapped air bubbles. The slurries were later cast over silicone sprayed stainless steel and pulled across the casting bed at a speed of 16 cm/min, adjusting the doctor blade height at 1 mm. After casting the tapes were transferred into a separate freeze dryer whose freezing plate temperature had been previously set at −45 °C. Once the slurries were completely frozen, the ice crystals were sublimated imposing low vacuum in the freezing chamber while the temperature returned to 15 °C.

After water sublimation, the tapes were removed from the freeze dryer and circular samples were cut out using a hollow steel punch. Further details on the manufacturing steps and influence of the main operating parameters over the resulting scaffold morphology can be found in Ref. [40].

The production of electrolyte-supported samples required the shaping of button pellets of 8YSZ (TZ-8Y, Tosoh Corporation) which were fabricated by the uniaxial die pressing (40 MPa) of the commercial powders followed by the sintering of the obtained green pellets at 1400 °C for 2 h. The adhesion between the sintered 8YSZ disks and the green porous backbones of GDC10 and 8YSZ was attained by screen printing an adhesive paste made out of a mixture of GDC10/8YSZ − α-therpineol (Sigma Aldrich) over the electrolyte.

Eventually, GDC10 and 8YSZ freeze tape cast backbones were repeatedly impregnated with a 2 M water-based solution of $Ni(NO_3)_2$ (Sigma Aldrich) where 1.5 wt% of a non-ionic surfactant, Triton X-100 (Sigma Aldrich), was added to increase the solid surface wettability. After every infiltration cycle, the samples were treated at high temperature (T>200 °C) to convert the Ni nitrate in Ni oxide, remove water and facilitate further electrocatalyst loading up to reaching the 15% of the initial backbone weight. The resulting samples were sintered at 1350 °C for 2 h in ambient air, setting a heating ramp of 1 °C/min and two dwelling steps of 1 h at 550 °C and 1000 °C, respectively. The tested cells were then reduced at 700 °C under pure H_2 for 12 h.

Table 1 – Composition, expressed as volume ratio percentages, of the GDC10/8YSZ-based starting suspension for the manufacturing of freeze tape cast scaffolds.

Components	(vol%/vol%)
Water	54.50%
Dispersant	2.85%
GDC10/8YSZ	16.20%
Surfynol SE-F	0.15%
Acrylic Emulsion Binder	26%
Arabic Gum	0.30%

2.2. Morphological and electrochemical characterization

The microstructure of the sintered GDC10 and 8YSZ backbones was investigated by SEM micrographs (ZEISS Ultra 55 instrument with a field emission gun, FEG), embedding the cross sections under vacuum in epoxy resin and polishing them down to 0.25 μm finish. The morphological properties of the freeze tape cast backbones were also analyzed by an X-Ray micro-tomography to perform the volumetric reconstruction of an extracted Volume of Interest (VOI) from the backbone architecture. This latter characterisation was carried out with a Zeiss Xradia 510 Versa Microscope using a voxel size of $1.9\times1.9\times1.9\ \mu m^3$ and obtaining 2400 projections of the sample.

The software MATLAB R2021 was then employed to extract the volumetric fractions of porosity and solid phase by performing the segmentation of a selected 3D matrix and computing the number fraction of porosity and GDC10 in the analyzed sub volume. Furthermore, the tortuosity factors of porosity and solid phases (τ) were estimated with the MATLAB application TauFactor which calculates the τ parameter using an over relaxed finite-different approach [41].

The electrochemical analyses were carried out testing symmetrical samples in a commercial test rig, ProboStat™ high temperature test fixture, devised for the electrochemical investigation of button cells. The schematic illustration of the sample holder in the experimental test bench is reported in Figure S.M. 1. The tested samples featured an active area of 1 cm^2 and two platinum nets deposited over the working and counter electrodes surfaces to optimize the electrical contact. A Ni paste was also applied between the surface of the backbones and the platinum grids to facilitate the current distribution. The electrochemical properties of the samples were evaluated by EIS, performing measurements in a two electrodes configuration. EIS data were obtained applying a sinusoidal perturbation of 10 mV to the system over the frequency range 10^5–10^{-1} Hz, generated by the workstation PGSTAT302 N from Autolab, METROHM, recording twelve points per decade of frequency. The measurements were taken at open circuit voltage (OCV) in the operating temperature range 600–750 °C with a temperature step of 25 °C. Prior starting the investigations, the linearity of the current response to the input voltage perturbation was checked. The voltage perturbation amplitude was swept in the 5–50 mV range, with the purpose of assessing if the current perturbation was varying linearly with the voltage one, thus verifying if the measured impedance was independent of the voltage perturbation amplitude [42]. Short circuit measurements of the cell rig were taken under the same conditions of the impedance analyses to correct the inductance in the impedance spectra [43]. A Kramers-Kronig test was also applied to the data to ensure the validity of the measured spectra [44]. The electrochemical investigation is supported by the construction of an EC model. The EC model is developed after performing the DRT analysis on the impedance spectra and is based on the physical interpretation of the observed resistive mechanisms.

3. Results and discussion

3.1. 3D reconstruction and morphological characterization

The microstructure of the Ni – impregnated GDC10 electrodes is reported in Fig. 1 a – d, which highlight the graded porosity of the ~550–600 μm freeze tape cast scaffolds (Fig. 1 a), the infiltrated porous interlayer (Fig. 1 b) and the distribution of the Ni phase by SEM and EDX analysis (Fig. 1 c-d). The analogous microstructure obtained for the manufactured 8YSZ freeze tape cast scaffolds was previously introduced in Ref. [40]. Fig. 1 c - d outline the heterogenous size of the Ni nanoparticles, holding a characteristic diameter which ranges from a minimum of 200 nm in the porous interlayer to values higher than 1 μm within the graded electrode. The presence of a bimodal distribution for the electrocatalyst size is likely due to the morphological properties of the scaffold and the adopted manufacturing method. The freeze tape cast backbones walls show micro-pores which accommodate the penetration of the initial $Ni(NO_3)_2$ – precursor solution within the bulk of the scaffold and the subsequent generation of Ni nanoparticles therein. The hindrance effect of the smaller characteristic porosity of the interlayer, instead, limits the growth of the Ni nanoparticles compared to both the functional and supporting layer of the backbone, thus creating a bimodal distribution. The presence of Ni clusters is also promoted by the adopted firing procedure in which the green Ni-impregnated GDC10 scaffold was co-sintered at 1300 °C. The high temperature treatment brought the Ni impregnated phase to a higher calcination temperature compared to the one reached in conventional infiltration procedures where the electrocatalyst is fired at 800–900 °C to obtain nanoparticles holding a diameter in the 50–100 nm range [12,15,22,45]. However, the expected presence of larger Ni nanoparticles was regarded as an acceptable trade-off to minimize the number of thermal treatments for the electrode shaping (in view of a potential scale up of the manufacturing method) and strengthen the bonding between the GDC10 substrate and the Ni nanoparticles.

The high-volume percentage and anisotropy of scaffold porosity (cf. Fig. 1 a) promoted the penetration of the $Ni(NO_3)_2$ – precursor solution up to the interface with the electrolyte, thus highlighting the effectiveness of the impregnation method within a graded porous microstructure. On the other hand, the large amount of pores within the sintered electrode bulk is expected to affect its mechanical robustness, thus calling for the increase of the starting suspension solid loading. The suspension composition reported in Table 1 features a consistent volume percentage of solvent and organics to be removed during the lyophilization and sintering processes. However, it was initially selected because it holds the desired rheological properties for the tape casting deposition and imparts enough flexibility and workability to the freeze-dried tapes.

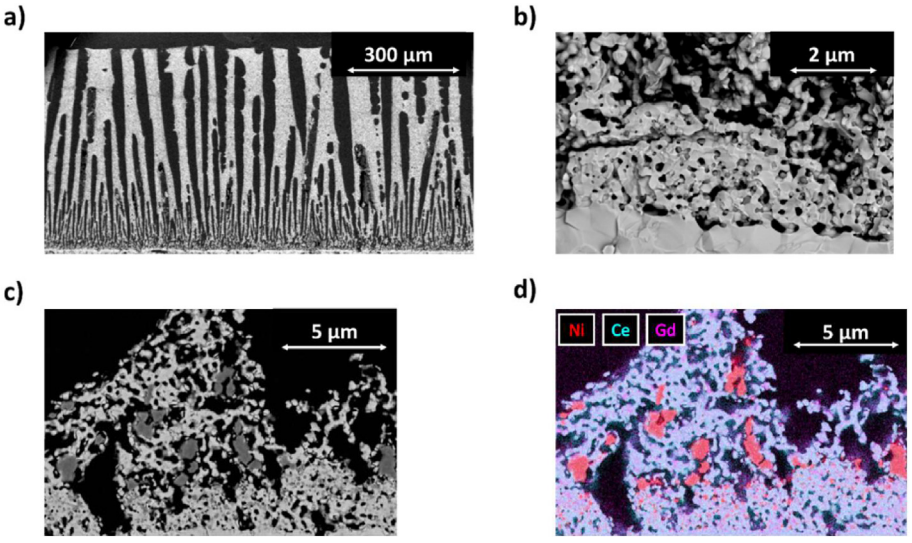

Fig. 1 – a) SEM micrograph of the cross section of the sintered impregnated GDC10 backbone; b): SEM micrograph highlighting the infiltrated porous interlayer; c): SEM cross sections of the impregnated GDC10 functional layers; d): EDX analysis on the cross sections of infiltrated GDC10 highlighting the bimodal distribution of Ni.

The unique morphology of the freeze tape cast backbones was also characterized by means of X-Ray micro-tomography and Fig. 2 a - c show a Region of Interest (ROI) which was extracted from the whole reconstruction of the freeze tape cast GDC10 backbone. A representative volume size of 600×600×300 μm^3 has been selected to visualize the 3D reconstruction of the scaffold.

The volumetric microstructure has been reconstructed using a voxel size of 1.9×1.9×1.9 μm^3 by directly stacking the raw X-ray gray images along the y-axis in sequence. The two phases of the backbones can be identified by the light blue (porous phase) and red (solid phase) colors. Before analyzing the electrode microstructural properties, the stack of 2D images has been segmented by labeling the solid and pore phases. The ImageJ software was employed to apply the Otsu method to label the two different phases after the identification of lower and higher thresholds [46].

The ROI reported in Fig. 2 a was also used to compute the microstructural properties of the freeze tape cast backbone. The z coordinate of the sub volume ranges from 80 to 380 µm, thus excluding both the bottom part of the scaffold (i.e. the functional layer) due to the lower resolution of the images obtained with the 1.9×1.9×1.9 μm^3 voxel size. Therefore, the microstructural analyses investigated the middle-high part of the backbone (diffusion layer) focusing on the calculation of the volume fraction (V_f) and mean radii ($\bar{r}_i$) of the two phases and their respective tortuosity factors (τ). The latter, in particular, is regarded as one of the most important parameters in the mass transfer process within porous materials, playing a key role on the gas diffusion [47,48]. The tortuosity factor of a conducting phase (i.e. 8YSZ/GDC10 for the ionic transport or hierarchical porosity for gas diffusion) is usually defined as (Eq. (1)):

$$\tau = V_f \frac{\sigma_i}{\sigma_i^{eff}} \quad [1]$$

where σ_i is the conductivity or diffusivity of the single conducting phase, and σ_i^{eff} is the effective conductivity or diffusivity of the porous medium. The V_f values of porosity and solid phases have been extracted from the segmented 3D matrix by computing on MatlabR2021b the number fraction of porosity and GDC10 voxels in the 3D sub volume. On the other

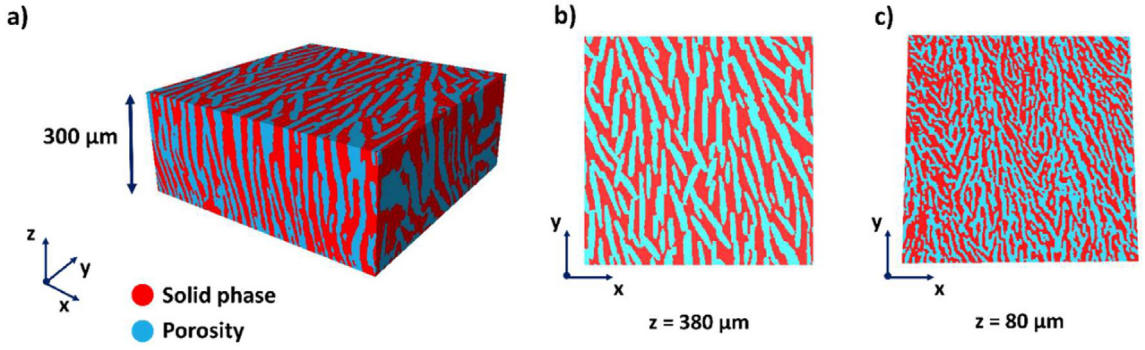

Fig. 2 – a) 3D reconstruction of a 600 × 600 × 300 GDC10 ROI showing the solid and porous phases; b) Top view of the GDC10 ROI (z = 380 µm); c) Bottom view of the GDC ROI (z = 80 µm).

hand, $\bar{r}_i$ was estimated from statistical analyses of SEM micrographs while τ was calculated with the Matlab application TauFactor which calculates the τ parameter using an over relaxed finite-different approach [41].

Table 2 shows the calculated average values of the x, y and z components of τ (τ_x, τ_y, τ_z), V_f and $\bar{r}_i$ for the solid and porous phases.

Along the z direction, τ_z average values of 1.38 and 1.17 are calculated for porosity and solid phase, respectively, being considerably smaller than both τ_x and τ_y of the corresponding conducting phases. These results outline the large anisotropy of the manufactured scaffolds which is expected to boost the species conduction across the scaffold thickness. In particular, the impact of the τ_z value of the porous phase, which is found to be exceptionally lower if compared to the results commonly reported for conventional sponge-like electrodes (~2–20 [46,49,50]), is expected to drop the diffusion resistance (R_{diff}) during operation. The 1D R_{diff} in a SOFC anode can be estimated as (Eq. (2)) [51]:

$$R_{diff} = \left(\frac{RT}{nF}\right)^2 \frac{1}{Dp_{ref}} L \frac{\tau}{V_{f,por}} \quad [2]$$

where n is the number of electrons involved in the redox reaction, F the Faraday constant, D the diffusion coefficient, p_{ref} the reference pressure, L the thickness of the electrode and $V_{f,por}$ the volumetric percentage of porosity. Eq. (2) shows that R_{diff} is dependent both on τ and $V_{f,por}$ suggesting that an insufficient volumetric fraction of porosity combined to a high tortuosity factor can increase R_{diff}, thus hindering the overall electrochemical performance. Furthermore, the value of τ impacts the activation overvoltage, due to the dependency of the current density from the reactant surface concentration, c_r, which can be expressed as [52], Eq. (3):

$$c_r = c_{r0} - \frac{i}{nFD} L \frac{\tau}{\varepsilon} \quad [3]$$

where c_{r0} is the reactant concentration in the flow channel.

The directional porosity is expected to reduce the concentration gradient between the gas flow channels and the active sites, leading to a small mismatch between c_r and c_r, thus accelerating the reaction rate and increasing the electrochemical performance.

3.2. Electrochemical tests

The microstructural characterization of the scaffold supported the electrochemical investigation of symmetrical electrolyte-supported cells by EIS. In particular, the extracted τ_z, V_f and $\bar{r}_{pores}$ were initially used to evaluate the characteristic R_{diff} of the manufactured freeze tape cast backbones. The EIS data of standalone GDC10, Ni-impregnated GDC10 and 8YSZ are then compared at 750 °C to evaluate the impact of the electrodes materials in the graded porous architecture.

Table 2 – Volume fraction and calculated tortuosity factors on the x, y and z directions for the porous and solid phases.

	τ_x	τ_y	τ_z	V_f	$\bar{r}$
Porosity	10.2	6.87	1.38	0.45	6.21
Solid Phase	7.47	3.45	1.17	0.55	9.16

The manufacturing of freeze tape cast porous backbones, holding a thickness of ~550–600 μm after sintering, is expected to hinder the performance of the electrodes due to ionic conduction limitations, which directly scale with the electrode thickness. GDC10 is known to be as a two-three times better ion conducting material than YSZ in the operating temperature range between 700 and 800 °C, thus reducing the ohmic contribution of the polarization resistance (Rp) [53–55]. Furthermore, the demonstrated mixed ionic-electronic conductivity (MIEC) shown by doped ceria in reducing atmosphere can partially support the transport of electrons [56,57]. Then, unlike Ni-YSZ fuel electrodes where YSZ acts as a pure ionic conductor, in Ni-GDC10 active layers the charge transfer reactions are no longer confined to the triple phase boundary (TPB) sites but extend to the whole GDC10 reactive surface [51,58,59]. Because of the reported electrochemical activity and viability of standalone GDC10 fuel electrodes [60], the effect of the Ni phase addition was also evaluated comparing the performance of Ni-impregnated and pure GDC10 freeze tape cast supports.

3.2.1. Diffusion resistance in freeze tape cast scaffolds

The quantification of the precise impact of the R_{diff} on the global polarization resistance of freeze tape cast electrodes holds a major relevance to evaluate if the hierarchical porous architecture provides the expected benefits to the gas diffusion process. The 1D expression to calculate the average R_{diff} in a SOFC anode is reported in Eq. (2). The diffusion coefficient D for a multi-component gas atmosphere including H_2, H_2O and N_2 as diluent is calculated taking into account the binary diffusion coefficients ($D_{i\text{-}j}$), derived from the Fuller's theory [46] and the Knudsen diffusion coefficient ($D_{K,i}$), Eq. (4) and Eq. (5):

$$D_{K,i} = \bar{r}_{por} \frac{2}{3} \sqrt{\frac{8 \cdot 1000 \cdot RT}{\pi m_i}} \quad [4]$$

$$D_{i-j} = \frac{0.00143}{P_{tot}\left(\sqrt[3]{V_i} + \sqrt[3]{V_j}\right)^2 \sqrt{\frac{2}{\frac{1}{m_i}+\frac{1}{m_j}}}} T^{1.75} 10^{-4} \quad [5]$$

where $\bar{r}_{pores}$ is taken from Table 2, m_i is the molar mass of the i-th species and V_i is the Fuller volume of the i-th species. The calculation of the R_{diff} value was then carried out calculating D by the Bosanquet formula [27,46] and using the τ and $V_{f,por}$ values reported in Table 2. It must also be pointed out that the calculation of R_{diff} was performed taking into account the large anisotropy of the freeze tape cast scaffold and considering the z axis as the preferential diffusion direction.

Fig. 3 shows the linear scale between R_{diff} and $T^{0.25}$ in the 600–750 °C temperature range.

The observed linear relationship between R_{diff} and $T^{0.25}$ (Fig. 3) suggests that the main contribution to the overall diffusion coefficient is provided by $D_{i\text{-}j}$ (which depends from $T^{1.75}$, Eq. (5)), thus hinting that $D_{K,i}$ can be neglected. The calculation of the Knudsen number, carried out to identify the governing mechanism in the gas diffusion regime, returned values lower than 0.1 in the whole investigated temperature range, confirming the negligible impact of Knudsen diffusion

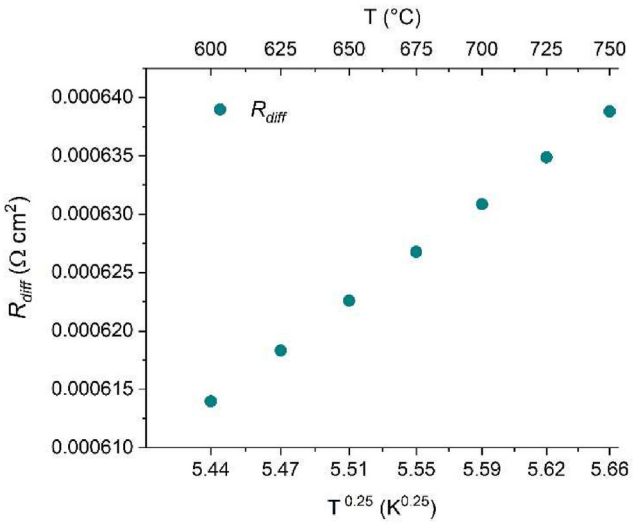

Fig. 3 – R_{diff} as function of temperature between 600 and 750 °C.

in the manufactured freeze tape cast electrodes [61]. The large sized pores and the oriented hierarchical gas diffusion of the GDC10 backbones boost the inflow and outflow of the gases within the electrode leading to exceptionally low R_{diff} values compared to the state-of-the-art sponge-like electrodes which, to the authors knowledge, have been reported to show R_{diff} values in the 1–50 mΩ cm^2 range for the best-case scenarios [51,58,62].

3.2.2. *Electrochemical comparison of single GDC10, Ni-infiltrated GDC10 and 8YSZ freeze tape cast fuel electrodes*

The benefits provided by hierarchical porosity to R_{diff} stem from the microstructural characteristics of the freeze tape cast scaffold and can then be considered independent from the electrode materials. For this reason, graded porous standalone GDC10, Ni-infiltrated GDC10 and Ni-infiltrated 8YSZ were electrochemically characterized to assess the behavior of conventional SOCs fuel electrode materials in the nanostructured hierarchical porous microstructure. Specifically, the samples were tested at 750 °C, at OCV, feeding 80% of humid H_2 (97% H_2–3% H_2O) as fuel and 20% of N_2 as carrier gas. The electrochemical comparison between the three manufactured electrodes in terms of Nyquist plots is presented in Fig. 4 a. The investigation of their electrochemical behavior was also integrated by the DRT technique with the purpose of supporting the analysis of the Nyquist spectra. The DRT approach is regarded to provide a deeper insight into the interpretation of the EIS data by performing the deconvolution of the main resistive contributions and the identification of their characteristic relaxation times. In this work, an in-house developed procedure, namely extended domain distribution of relaxation times (ED-DRT), was adopted [63]. Its application on EIS data enables the extension of the frequency values beyond the experimental frequency range thanks to the zero padding technique, thus promoting the analysis of EIS data whose imaginary component does not approach zero at the experimental frequency bounds. The electrodes Rp were estimated from the integration of the corresponding DRT curves (Fig. 4 b) rather than from the intersection of the experimental data with the real component in the Nyquist plots.

The obtained Rp values were equal to 6.98 Ω cm^2 for the Ni-infiltrated 8YSZ scaffold, 3.02 Ω cm^2 for pure GDC10 and 0.823 Ω cm^2 for the Ni-infiltrated GDC10 electrode. The high Rp of the Ni-infiltrated 8YSZ scaffold is mainly addressed to the impregnation procedure and electrode architecture. Indeed, it is envisaged that the addition of Ni nanoparticles over pure 8YSZ does not provide the electrode with sufficient electrons conducting properties. The scattered distribution of the Ni phase obtained by experimental infiltration (cf. Fig. 1) does not create a low tortuous and homogeneous nanolayer of Ni over the 8YSZ scaffold surface. The combination of the high tortuosity factor of the connected Ni nanoparticles and low $V_{f,Ni}$ compared to traditional Ni-8YSZ cermets, can significantly impact the effective electronic conductivity according to Eq. (6):

$$\sigma_{Ni}^{eff} = \frac{V_{f,Ni}}{\tau_{Ni}}\sigma_{Ni} \quad [6]$$

where σ_{Ni} is the bulk electronic conductivity of Ni.

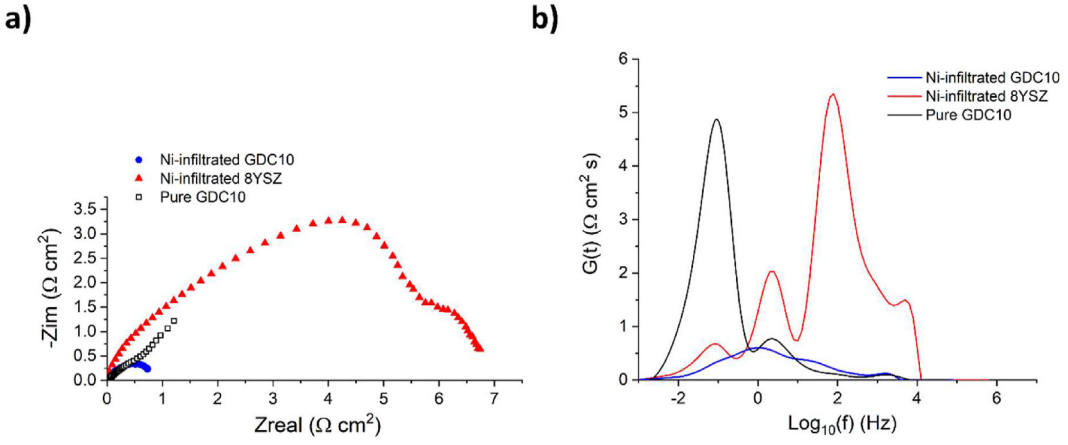

Fig. 4 – a)-b) Nyquist plot and corresponding DRT spectra, at 750 °C and OCV, of Ni-infiltrated GDC10, standalone GDC10 and Ni-infiltrated 8YSZ.

The DRT of the Ni-infiltrated 8YSZ scaffold (Fig. 4 b) shows a high resistive peak, holding a characteristic frequency of 125.6 Hz, which is addressed to the low reactivity of the electrode. In particular, it was previously reported that the DRT charge transfer peak of Ni-YSZ cermets can be found in the 10^3 Hz frequency decade, being then characterized by a lower relaxation time [62,64]. The observed shift to a lower frequency in the nanostructured freeze tape cast electrode is specifically attributed to the tortuosity factor of the discrete Ni phase. Indeed, a high tortuosity distribution of Ni particles along the scaffold can generate a resistance to the migration of charged species lowering the electrode reactivity [65]. On the other hand, when using a GDC10 scaffold, the MIEC properties of ceria under reducing conditions support the global electronic conductivity of the electrode. However, the impedance spectra measured on the pure GDC10 freeze tape cast architecture suggest that the only electron conducting properties of ceria are not high enough to sustain the whole electronic migration. Specifically, Fig. 4 a evidences a high resistive contribution at low frequencies whose shape is typically associated with diffusion limitations and fitted with a Warburg element in EC modelling [62,64,66]. In particular, it is envisioned that the high thickness of the manufactured freeze tape cast scaffolds (~550–600 μm) and the absence of a pure electronic conductor inhibit the effective electronic conductivity. The high electrochemical performance of pure GDC10 as fuel electrode reported in literature was measured in thin functional layers (~3–15 μm), thus minimizing the electrons transport path within the ceria bulk [60]. Therefore, in a thick supporting GDC10-based fuel electrode, the addition of Ni results to be necessary to boost the transport of the electrons, as confirmed by the lowest Rp (0.823 Ω cm^2) obtained for the Ni-infiltrated GDC10 architecture. This value is a very promising result considering both the overall thickness of the scaffold and the adopted testing conditions (97% H_2–3% H_2O). Indeed a higher pH_2O was previously determined to be beneficial to the kinetics of the low frequency process in Ni-GDC10 composite fuel electrode [58].

In light of the obtained results, the next sections deal with the investigation of the electrochemical behavior of the Ni-infiltrated GDC10 architecture, deconvoluting its underlying resistive mechanism to develop high performing Ni-ceria fuel electrodes with enhanced microstructural properties. To this end, the interpretation of EIS data has been supported by DRT analyses and EC modelling.

3.2.3. *Electrochemical properties of the freeze tape cast Ni-infiltrated GDC10 electrode*

3.2.3.1. *Temperature dependence*. Fig. 5 a shows the Nyquist plots taken in the temperature range 600–750 °C (focus at 750 °C in Fig. 5 b) in a mixed atmosphere of 80% humid H_2 (97% H_2–3% H_2O) as reactant and N_2 as inert gas (pN_2 20%). Fig. 5 c shows instead the corresponding Rp values as function of the operating temperature. The apparent resistive contribution of the electrode process is obtained by fitting the experimental data with the Arrhenius-type equation (Eq. 7):

$$R_p = Ae^{-E_a/RT} \quad [7]$$

where A is the pre-exponential factor, E_a the activation energy, R the universal constant of gases and T the temperature.

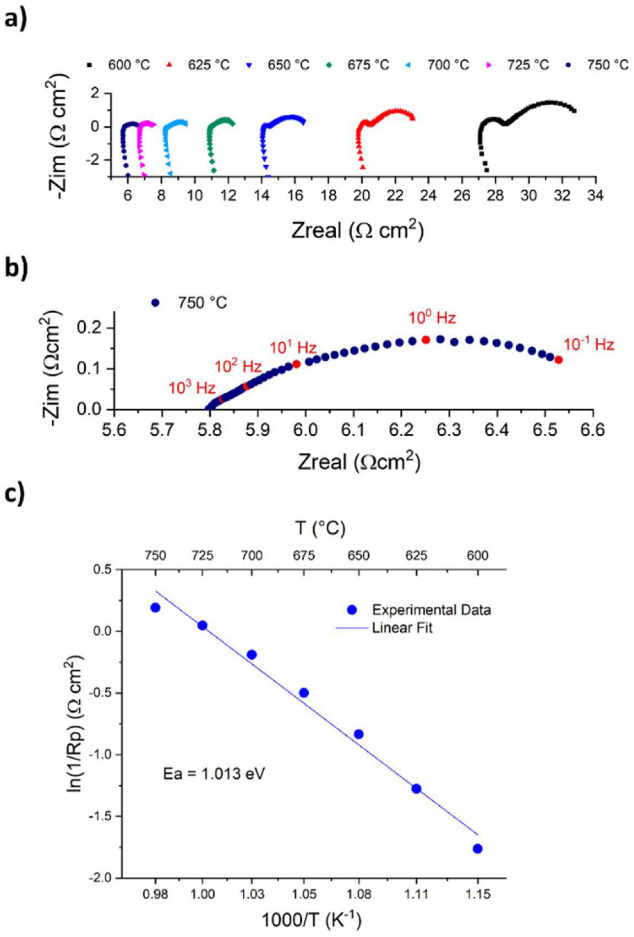

Fig. 5 – a) Nyquist plots in the temperature range 600–750 °C at OCV; b) Nyquist plot at 750 °C highlighting the decades of frequency; c) Corresponding Rp values in the Arrhenius-type plot.

The fit of the overall electrode resistive process shows a high quality, R^2>0.98, and yields a low activation energy barrier of 1.013 eV which outlines the high activity of the electrode towards the H_2 oxidation.

Fig. 5 a shows that the temperature increase reduces the ohmic resistive contribution, R_Ω, which is related to the migration of the O^{2-} ionic species throughout the lattice of the 8YSZ supporting electrolyte. The R_Ω is identified by the intercept of the curves with the Zreal axis at high frequencies and progressively shifts at lower Zreal values while increasing the operating temperature.

The measurements highlight the presence of at least two main resistive processes within the electrodes which, especially at low temperatures, can be identified by two distinguishable semicircles at different characteristic frequencies. The increase of the operating temperature lowers the Rp of the electrode and leads to the partial convolution of the two processes as shown in Fig. 5 b which focuses on the Nyquist plot at 750 °C. The investigation of the electrochemical behavior of the electrodes was also integrated with the DRT data (Fig. 6 a) calculated for the EIS measurements reported in Fig. 5 a. Two main contributions, one at low frequencies (LF) around 1 Hz and another at high frequencies (HF) around

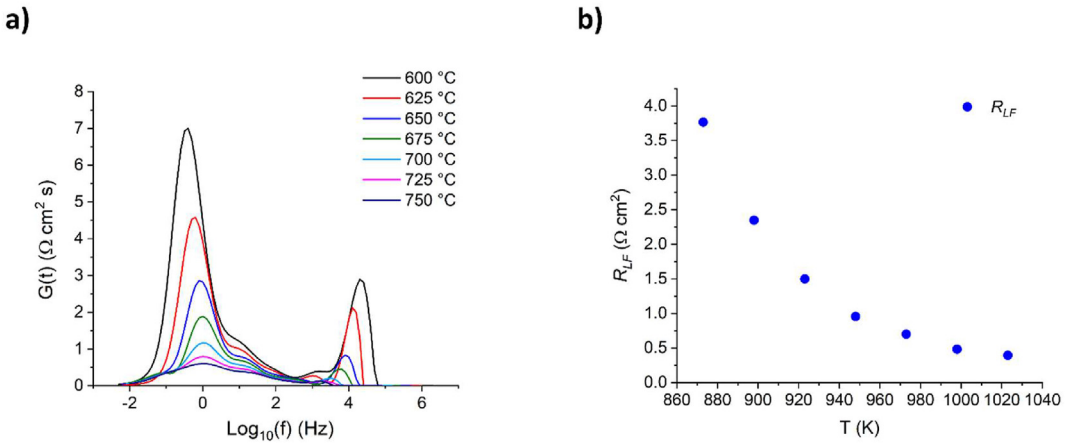

Fig. 6 – a) DRT of the impedance spectra varying the operating temperature in the range 600–750 °C; b) Evolution of R_{LF} as function of temperature.

10^4 Hz, can be distinguished from the DRT spectra. Both processes appear to be thermally activated, as shown by the decrease of the area under the peaks while increasing the operating temperature. They can thus be regarded as physico-chemical electrode processes. Two minor contributions at middle frequencies can also be identified, one around 10 Hz (MF1) and another around 10^3 Hz (MF2). However, initially, they have not been included in the proposed EC fitting model due to their apparent lower impact on the overall Rp compared to the LF and HF processes. The LF contribution appears to be the limiting one at every operating temperature and, according to its characteristic frequency, can be ascribed to surface processes such as H_2 adsorption accompanied by surface diffusion [67]. The contribution of gas diffusion is also usually observed in the same frequency range [62,64], but its impact has been found negligible in the freeze tape cast architecture (cf. Fig. 3). Fig. 6 b shows the evolution of the resistance of the LF contribution (R_{LF}) as function of temperature, calculated as the integral of the LF peak from the DRT spectra.

The origin of the LF resistive process could then be searched into the surface activity of GDC10 towards the oxidation of H_2 in reducing atmosphere, where GDC10 becomes a MIEC material. In previous studies on Ni-GDC cermets holding conventional microstructure, the mixed valence of Ce between Ce^{3+}/Ce^{4+} was ascribed to be responsible for the formation of a surface/gas double layer and the occurrence of a chemical capacitance, C_{chem}, within the GDC lattice [51,58,68]. It was previously reported that, on the surface of a MIEC, an electrostatic potential step is generated by the presence of a double layer established by the accumulation of negative adsorbed species and positive electronic counter charges [69]. When an inlet gas of H_2/H_2O is fed to a GDC-based electrode, a surface potential step is created by the variation of the concentration of the surface adsorbed species and the Ce^{3+}/Ce^{4+} ratio, according to (Eq. (8)) [67]:

$$2Ce_{Ce}^{x} + O_{O}^{x} \leftrightarrow 2Ce'_{Ce} + V_{\ddot{O}} + H_2O \quad [8]$$

The surface reduction of GDC in reducing atmosphere can thus lead to the formation of oxygen vacancies and a mixed valence Ce^{3+}/Ce^{4+} which generates C_{chem}.

Based on the EIS data and DRT analysis, an EC model including L1-Rel-(RLF//CPE LF)-(RHF//CPE HF) was employed with the purpose of fitting the experimental data. The L1 element models the inducting behavior of the Pt wires, Rel the ohmic resistance of the supporting electrolyte, while the two -(R//CPE)- elements are adopted to fit the LF and HF processes. A simple capacitor is here replaced by a constant phase element (CPE) to take into account the broad peak shapes of the LF and HF processes in the DRT spectra, which might recall a dispersion of time constants of multiple reaction processes or heterogeneities at solid interfaces [66,70]. Fig. 7 a shows the good agreement between the experimental data and the EC model at 750 °C. The accuracy of the EC fitting is furtherly proved by the accordance between the characteristic frequencies of the controlling LF and HF mechanisms, Fig. 7 b.

Starting from the CPE values obtained from the fitting procedure, the equivalent capacities (C_{eq}) were estimated according to (Eq. (9)) [71,72]:

$$C_{eq} = R^{1-n/n} Q^{1/n} \quad [9]$$

where R is the resistance of the -(R//CPE)- subcircuit and Q and n are the module and exponential parameter of the CPE element. The characteristic frequencies of the LF and HF processes were subsequently calculated as (Eq. (10)):

$$f = \frac{1}{2\pi R C_{eq}} \quad [10]$$

The estimated C_{eq} values related to the LF process express the C_{chem} of GDC10 and were found to be larger than those typically associated with the electric double layers generated at the interfaces between Ni and YSZ in Ni-YSZ cermet electrodes [58]. Fig. 8 shows the dependence of the LF C_{eq} from the operating temperature.

The LF C_{eq} values increase while increasing the operating temperature and stretch in the 0.06–0.12 F cm^{-2} range, thus being 2–3 order of magnitude larger than the C_{eq} values obtained for the Ni-YSZ cermets [58]. The results obtained from the EIS data analysis suggest a different H_2 oxidation mechanism taking place in Ni-GDC electrodes and related to the extension of the electrochemical reactive zone from the TPB

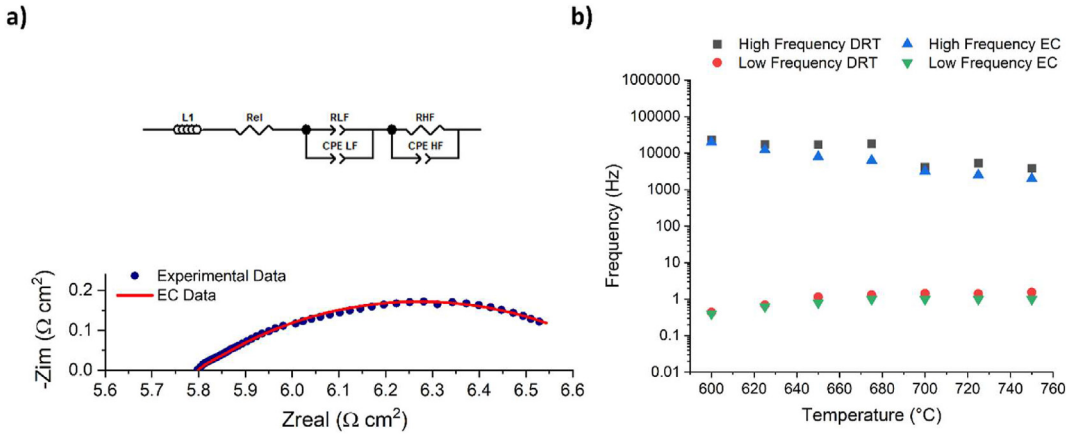

Fig. 7 – a) CNLS fitting with the L1-Rel-(RLF//CPE LF)-(RHF//CPE HF) EC model shown with the experimental Nyquist plot. b) Characteristic frequencies of the LF and HF processes as function of the operating temperature identified by DRT and EC fit.

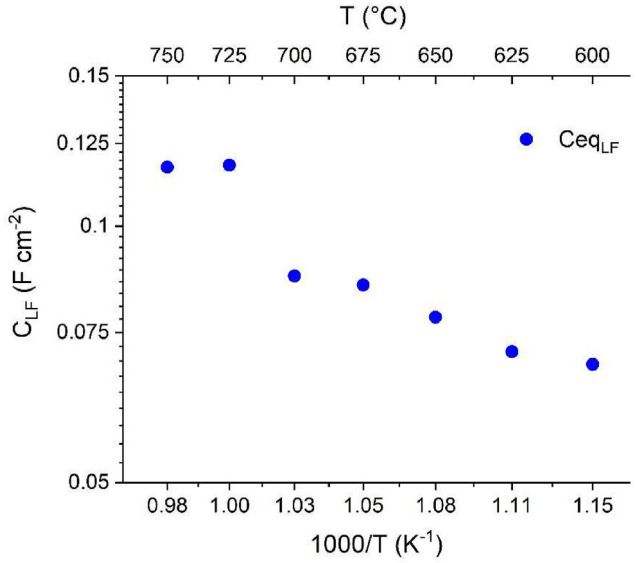

Fig. 8 – Variation of the LF C_{eq} as function of the operating temperature.

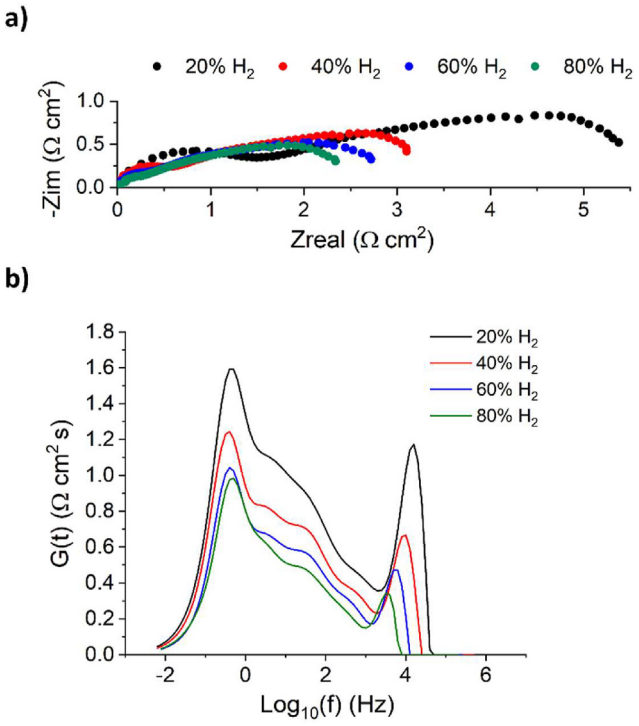

Fig. 9 – a) Nyquist plots at 700 °C varying pH_2; b) Corresponding DRT spectra highlighting the evolution of the main resistive contributions of Rp with a different fuel percentage.

sites of Ni-YSZ to the double phase boundary (DPB) electrode surface area - gas phase of the Ni-GDC cermet. The electro-oxidation process is regarded to be shifted from frequencies in the range 10^3–10^4 Hz in Ni-YSZ fuel electrodes to 1 Hz in Ni-GDC electrodes due to the large C_{chem} originating from the oxygen non-stoichiometry of the GDC10 lattice. It must also be stressed, as already shown in the model of Adler [73], that the C_{chem} of a MIEC is associated with its bulk oxidation/reduction, thus explaining why the C_{eq} values obtained from the EC model result to be order of magnitudes larger than surface or inter-facial capacitance ones. Therefore, the limiting step of the electrochemical process can be either a surface phenomenon, such as the adsorption/desorption of chemical species, or a bulk one like the accumulation of reactive intermediates within the GDC10 bulk due to the slow transport of charged species.

3.2.3.2. *Partial pressure dependence*. The influence of the fuel partial pressure on the electrochemical behavior of the Ni-GDC freeze cast electrodes was also investigated by changing pH_2, keeping the pH_2/pH_2O ratio constant to 97%/3%. Fig. 9 a - b show the Nyquist plots and the corresponding DRT spectra at 700 °C, considered as a plausible operating temperature for Ni-GDC fuel electrodes due to the higher ionic conducting properties of doped ceria compared to the state-of-the-art YSZ [74,75].

The EIS results show that a larger reducing atmosphere promotes the decrease of the polarization resistance, acting on the two main physico-chemical processes highlighted by the DRT spectra. From Fig. 9 b it can be noted that the variation

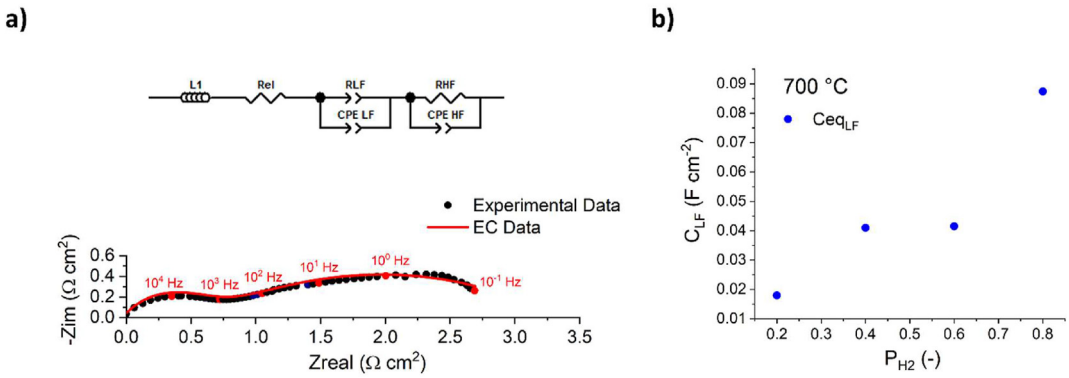

Fig. 10 – a) EC fitting with the L1-Rel-(RLF//CPE LF)-(RHF//CPE HF) model shown over the Nyquist plot. b) Variation of the calculated LF C_{eq} with the operating temperature.

of pH_2 does not shift the characteristic frequency of the LF process but highlights the contribution of its peak shoulder, namely MF1. In previous works on Ni-GDC fuel electrodes, the presence of a middle frequency process (10^1–10^2 Hz) was ascribed to the transport of oxygen ions throughout the MIEC lattice [58,68], thus confirming, as previously discussed, that the electrochemical process might be limited either by a surface or bulk mechanism. It must also be pointed out that the DRT analysis at different operating temperature outlined the progressive broadening of the LF peak while increasing the operating temperature, which could also suggest a physical-based link between the underlying processes of LF and MF1.

The EC model introduced in 3.2.3.1 was employed to fit the EIS data at different partial pressures. Fig. 10 a shows, once again, the obtained good accordance between the EC model and the experimental data at 700 °C with 80% pH_2 while Fig. 10 b reports the variation of the extracted LF C_{eq} values as function of pH_2.

The increase of pH_2 enhances the C_{eq} of LF, thus suggesting that the extension of the electrochemical process throughout the electrode volume is controlled by the severity of the reducing environment. Indeed, a higher pH_2 is expected to enhance the Ce^{3+} bulk concentration and, consequently, the chemical capacitance of the electrode.

An alternative approach to the construction of the EC model can follow the findings reported in previous studies on MIECs, where the surface phenomena connected to charge transfer and the species migration within the bulk were simulated by a Gerischer element (-G-) [66,73,76]. In particular, the physical interpretation of the LF peak leads the authors to suggest an alternative EC model (L1-Rel-G-(RHF//CPE HF)-) to the one introduced in Section 3.2.3.1, substituting the -(RLF//CPE LF)- subcircuit with -G- to take into account the MIEC properties of GDC10 in a reducing atmosphere. The good agreement between the second EC model proposed and the experimental data is reported in supporting material (Figure S.M.2). The good fit obtained with the use of the -G- element furtherly confirms the performance colimitation due either to the charge transfer reaction or charge transport. Specifically, according to the model of Adler [73], the half-teardrop shape of the LF resistive process in the Nyquist plot, highlights that the electrode is mainly limited by the transport of charged species through the bulk of GDC10. In general, the analyses of the EIS data evidence the slow transport of charged species within the Ni-impregnated GDC10 electrode due both to the high thickness of the ceria scaffold and inhomogeneous distribution of the Ni phase.

The employment of a -(R//CPE)- subcircuit is maintained for the HF peaks which are largely dependent on both temperature and pH_2, shifting at lower frequencies while increasing the operating parameters. In conventional sponge-like Ni-GDC electrodes no resistive processes were identified over 10^2–10^3 Hz, thus ascribing the whole limiting electrochemical mechanism to either the surface adsorption of chemical species or the O^{2-} migration within the GDC lattice [51,58,67,68].

In this work, the microstructure of the tested samples, where different layers consisting of an 8YSZ electrolyte, a GDC10 adhesion film and a thick GDC10 infiltrated backbone are stacked over each other, complicates the interpretation of the EIS data at high frequency. In particular, both the presence of a backbone largely thicker than conventional fuel electrodes and a solid interface between two different electrolyte materials (8YSZ-GDC10) are expected to slow down the migration of the O^{2-} species. Mo et al. [77] investigated the electrochemical behavior of a GDC-infiltrated Ni-YSZ cell and ascribed the presence of a high frequency contribution (10^4 Hz), dependent both from temperature and humidity level, to the GDC10/8YSZ interface grain boundary resistance. Accordingly, it is proposed that the HF resistive contribution stems from the multi-layered architecture of the tested symmetrical cells featuring an 8YSZ – GDC10 interlayer and GDC10 – Ni interfaces.

4. Conclusions

Hierarchical supporting fuel electrodes made out of a freeze tape cast GDC10 and 8YSZ scaffolds impregnated with Ni nanoparticles have been manufactured and characterized in this work to study their morphological and electrochemical properties.

The analysis of the microstructural parameters on the 3D reconstruction of the graded porous scaffold outlined the large anisotropy of the gas diffusion channels, showing a tortuosity factor on the out of plane direction significantly

smaller (τ_z=1.38) than the typical values of conventional sponge-like microstructures. The very low value calculated for the 1D gas diffusion resistance (~$6 \cdot 10^{-4}$ Ωcm^2 between 600 and 750 °C temperature range) outlines the benefits provided by hierarchical porosity in boosting mass transfer during operation. The electrochemical investigations on symmetrical electrolyte-supported button cells, featuring pure GDC10, Ni-impregnated GDC10 and 8YSZ freeze tape cast scaffolds, evidenced the higher electrochemical performance of the Ni-impregnated GDC10 architecture, holding an Rp of 0.823 Ω cm^2 at 750 °C compared to 6.98 Ω cm^2 and 3.02 Ω cm^2 of the Ni-infiltrated 8YSZ and pure GDC10, respectively. The analysis of the EIS data of the Ni-GDC10 architecture, led to the identification of two main resistive contributions, LF and HF, characterized by different relaxation times. The LF process has been ascribed to the occurrence of a C_{chem} within the GDC lattice in reducing environment, stretching in the range 0.06–0.12 Fcm^{-2} between 600 and 750 °C, which controls both the surface activity and charged species migration in the bulk of the electrode. On the other hand, it is suspected that the HF contribution originates from the multi-layered microstructure of the tested symmetrical cells and the presence of the interface GDC10/8YSZ which slows down the migration of the O^{2-} species.

The indications obtained from the electrochemical investigation encourage the manufacturing of freeze tape cast backbones characterized by lower overall thickness (~250 μm) and higher solid content (>20 vol%/vol%) to reduce the impact of the LF contribution and facilitate a more homogeneous distribution of the impregnated Ni nanoparticles. Indeed, the decrease of the backbone thickness can promote the higher percolation of the infiltrated nanoparticles and enhance the electronic migration throughout the Ni phase. As for the fuel electrode materials, the manufacturing of Ni-impregnated 8YSZ and pure GDC10 freeze tape cast electrodes is discouraged due to their insufficient electron conducting properties. The fabrication of optimized Ni-impregnated GDC10 freeze tape cast electrodes, holding higher Ni content and lower backbone thickness, is instead recommended due to the promising electrochemical properties measured on the tested samples.

Declaration of competing interest

The authors declare that they have no known competing financial interests or personal relationships that could have appeared to influence the work reported in this paper.

Acknowledgements

The authors want to thank Prof. Michael Schulz, Dr. Alex Gustschin and Dr. Yiyong Han from the Technical University of Munich (Germany) and Prof. Massimo Viviani and Dr. Juan Felipe Basbus from the Italian National Research Council (CNR-ICMATE) for they contribution to the X-Ray CT. The authors also acknowledge Dr. David Thomas, Dr. Maxime Hubert and Dr. Jerome Laurencin from the Univ. Grenoble Alpes – CEA/LITEN, Grenoble (France) for their contribution in the microstructural characterization of the Ni-GDC electrodes.

Eventually, the authors acknowledge the Italian project PROMETH2eus (*selezionato tra le attività di ricerca fondamentale nell'ambito dell'Investimento 3.5 "Ricerca e sviluppo sull'idrogeno", Missione 2 "Rivoluzione verde e transizione ecologica", Componente 2 "Energia rinnovabile, idrogeno, rete e mobilità sostenibile", del PNRR, finanziato dall'Unione europea – Next Generation Eu a valere sul decreto del Ministro della Transizione Ecologica del 23 Dicembre 2021, art. 1, comma 5, lettera A;* ID: RSH2B_000039 – CUP: F37G22000080006), coordinated by the department DICCA of the University of Genoa, which supported this work in view of the application of nanostructured graded porous electrodes in SOECs micro-stacks.

Appendix A. Supplementary data

Supplementary data to this article can be found online at https://doi.org/10.1016/j.ijhydene.2023.10.027.

REFERENCES

[1] Venkataraman V, Pérez-Fortes M, Wang L, Hajimolana YS, Boigues-Muñoz C, Agostini A, et al. Reversible solid oxide systems for energy and chemical applications – review & perspectives. J Energy Storage 2019;24:100782.
[2] Mogensen MB, Chen M, Frandsen HL, Graves C, Hansen JB, Hansen KV, et al. Reversible solid-oxide cells for clean and sustainable energy. Clean Energy 2019;3:175–201.
[3] Priya SD, Selvakumar AI, Nesaraj AS. Overview on ceramic and nanostructured materials for solid oxide fuel cells (SOFCs) working at different temperatures. J Electrochem Sci Technol 2020;11:99–116.
[4] Hagen A, Hendriksen PV. Progress of SOFC/SOEC development at DTU energy: from materials to systems. ECS Trans 2017;78:145.
[5] Mogensen MB. Materials for reversible solid oxide cells. Curr Opin Electrochem 2020;21:265–73.
[6] Molin S, Chrzan A, Karczewski J, Szymczewska D, Jasinski P. The role of thin functional layers in solid oxide fuel cells. Electrochim Acta 2016;204:136–45.
[7] Kagomiya I, Kaneko S, Yagi Y, Kakimoto K-i, Park K, Cho K-H. Dependence of power density on anode functional layer thickness in anode-supported solid oxide fuel cells. Ionics 2017;23:427–33.
[8] Nishihora RK, Rachadel PL, Quadri MGN, Hotza D. Manufacturing porous ceramic materials by tape casting—a review. J Eur Ceram Soc 2018;38:988–1001.
[9] Deepi AS, Dharani Priya S, Samson Nesaraj A, Selvakumar AI. Component fabrication techniques for solid oxide fuel cell (SOFC) – a comprehensive review and future prospects. Int J Green Energy 2022;19:1600–12.
[10] Mogensen MB, Chen M, Frandsen HL, Graves C, Hauch A, Hendriksen PV, et al. Ni migration in solid oxide cell electrodes: review and revised hypothesis. Fuel Cell 2021;21:415–29.
[11] Hauch A, Brodersen K, Chen M, Mogensen MB. Ni/YSZ electrodes structures optimized for increased electrolysis performance and durability. Solid State Ionics 2016;293:27–36.
[12] Tong X, Hendriksen PV, Hauch A, Sun X, Chen M. An up-scalable, infiltration-based approach for improving the

durability of Ni/YSZ electrodes for solid oxide cells. J Electrochem Soc 2020;167:24519.
[13] Jiang SP. Nanoscale and nano-structured electrodes of solid oxide fuel cells by infiltration: advances and challenges. Int J Hydrogen Energy 2012;37:449–70.
[14] Hołówko B, Karczewski J, Molin S, Jasiński P. Preparation of hydrogen electrodes of solid oxide cells by infiltration: effects of the preparation procedure on the resulting microstructure. Materials 2020;13:131.
[15] Dowd RP, Lee S, Fan Y, Gerdes K. Engineering the solid oxide fuel cell electrocatalyst infiltration technique for industrial use. Int J Hydrogen Energy 2016;41:14971–81.
[16] Cademartori D, Maria Asensio A, Clematis D, Basbus JF, Viviani M, Presto S, et al. A high-performance Co-free electrode for solid oxide cells: La0.7Sr0.3Cu0.15Fe0.85O3-δ synthesis and characterisation. J Alloys Compd 2023;965:171334.
[17] Zheng M, Wang S, Yang Y, Xia C. Barium carbonate as a synergistic catalyst for the H2O/CO2 reduction reaction at Ni–yttria stabilized zirconia cathodes for solid oxide electrolysis cells. J Mater Chem A 2018;6:2721–9.
[18] Ovtar S, Tong X, Bentzen JJ, Thydén KTS, Simonsen SB, Chen M. Boosting the performance and durability of Ni/YSZ cathode for hydrogen production at high current densities via decoration with nano-sized electrocatalysts. Nanoscale 2019;11:4394–406.
[19] Majnoni X, Cademartori D, Clematis D, Presto S, Viviani M, Botter R, et al. Infiltrated Ba0.5Sr0.5Co0.8Fe0.2O3-δ-Based electrodes as anodes in solid oxide electrolysis cells. Energies 2020;13:3659.
[20] Lu Y, Gasper P, Nikiforov AY, Pal UB, Gopalan S, Basu SN. Co-Infiltration of nickel and mixed conducting Gd0.1Ce0.9O2−δ and La0.6Sr0.3Ni0.15Cr0.85O3−δ phases in Ni-YSZ anodes for improved stability and performance. JOM 2019;71:3835–47.
[21] Develos-Bagarinao K, editor. Nanoengineered materials for solid oxide cells. IOP Publishing; 2023.
[22] Zakaria Z, Awang Mat Z, Abu Hassan SH, Boon Kar Y. A review of solid oxide fuel cell component fabrication methods toward lowering temperature. Int J Energy Res 2020;44:594–611.
[23] Snowdon AL, Jiang Z, Steinberger-Wilckens R. Five-layer reverse tape casting of IT-SOFC. Int J Appl Ceram Technol 2022;19:289–98.
[24] Sanson A, Pinasco P, Roncari E. Influence of pore formers on slurry composition and microstructure of tape cast supporting anodes for SOFCs. J Eur Ceram Soc 2008;28:1221–6.
[25] Chen X, Lin J, Sun L, Liu T, Wu J, Sheng Z, et al. Improvement of output performance of solid oxide fuel cell by optimizing the active anode functional layer. Electrochim Acta 2019;298:112–20.
[26] Kennouche D, Hong J, Noh H-S, Son J-W, Barnett SA. Three-dimensional microstructure of high-performance pulsed-laser deposited Ni–YSZ SOFC anodes. Phys Chem Chem Phys 2014;16:15249–55.
[27] Bertei A, Mertens J, Nicolella C. Electrochemical simulation of planar solid oxide fuel cells with detailed microstructural modeling. Electrochim Acta 2014;146:151–63.
[28] Wang Y, Li W, Ma L, Li W, Liu X. Degradation of solid oxide electrolysis cells: phenomena, mechanisms, and emerging mitigation strategies—a review. J Mater Sci Technol 2020;55:35–55.
[29] Khan MS, Xu X, Knibbe R, Zhu Z. Air electrodes and related degradation mechanisms in solid oxide electrolysis and reversible solid oxide cells. Renew Sustain Energy Rev 2021;143:110918.
[30] Ebbesen SD, Sun X, Mogensen MB. Understanding the processes governing performance and durability of solid oxide electrolysis cells. Faraday Discuss 2015;182:393–422.
[31] Hou M, Pan Y, He F, Xu K, Zhang H, Zhou Y, et al. Manipulating and optimizing the hierarchically porous electrode structures for rapid mass transport in solid oxide cells. Adv Funct Mater 2022;32:2203722.
[32] Sofie SW. Fabrication of functionally graded and aligned porosity in thin ceramic substrates with the novel freeze–tape-casting process. J Am Ceram Soc 2007;90:2024–31.
[33] Heywood SK, Romanenko K, Sofie SW, Codd SL. Intrinsic microstructural anisotropy in tape cast ceramics by ice templating. Int J Appl Ceram Technol 2020;17:2202–11.
[34] Chen Y, Liu Q, Yang Z, Chen F, Han M. High performance low temperature solid oxide fuel cells with novel electrode architecture. RSC Adv 2012;2:12118–21.
[35] Chen Y, Bunch J, Li T, Mao Z, Chen F. Novel functionally graded acicular electrode for solid oxide cells fabricated by the freeze-tape-casting process. J Power Sources 2012;213:93–9.
[36] Wu T, Zhang W, Yu B, Chen J. A novel electrolyte-electrode interface structure with directional micro-channel fabricated by freeze casting: a minireview. Int J Hydrogen Energy 2017;42:29900–10.
[37] Du Y, Hedayat N, Panthi D, Ilkhani H, Emley BJ, Woodson T. Freeze-casting for the fabrication of solid oxide fuel cells: a review. Materialia 2018;1:198–210.
[38] Chen Y, Zhang Y, Lin Y, Yang Z, Su D, Han M, et al. Direct-methane solid oxide fuel cells with hierarchically porous Ni-based anode deposited with nanocatalyst layer. Nano Energy 2014;10:1–9.
[39] Chen Y, Lin Y, Zhang Y, Wang S, Su D, Yang Z, et al. Low temperature solid oxide fuel cells with hierarchically porous cathode nano-network. Nano Energy 2014;8:25–33.
[40] Cademartori D, Mercadelli E, Gondolini A, Asensio AM, Bertei A, Sanson A, et al. Fabrication and electrochemical modelling of 8YSZ and GDC10 freeze tape cast scaffolds for solid oxide cells (SOCs). J Eur Ceram Soc 2023;43:5263–78.
[41] Cooper SJ, Bertei A, Shearing PR, Kilner JA, Brandon NP. TauFactor: an open-source application for calculating tortuosity factors from tomographic data. SoftwareX 2016;5:203–10.
[42] Barsoukov E, Macdonald JR. Impedance spectroscopy: theory, experiment, and applications. 2005.
[43] Akter A, Mulligan JR, Lee J-I, Pal U, Basu S, Gopalan S. Correcting for inductance in low-impedance electrochemical systems. JOM 2022;74:4544–50.
[44] Schönleber M, Klotz D, Ivers-Tiffée E. A method for improving the robustness of linear kramers-kronig validity tests. Electrochim Acta 2014;131:20–7.
[45] Asensio AM, Clematis D, Viviani M, Carpanese MP, Presto S, Cademartori D, et al. Impregnation of microporous SDC scaffold as stable solid oxide cell BSCF-based air electrode. Energy 2021;237:121514.
[46] Monaco F, Effori E, Hubert M, Siebert E, Geneste G, Morel B, et al. Electrode kinetics of porous Ni-3YSZ cermet operated in fuel cell and electrolysis modes for solid oxide cell application. Electrochim Acta 2021;389:138765.
[47] Zheng K, Zhang Y, Li L, Ni M. On the tortuosity factor of solid phase in solid oxide fuel cell electrodes. Int J Hydrogen Energy 2015;40:665–9.
[48] Zheng K, Li L, Shen S, Wang S. The tortuosity factor effect on solid oxide fuel cell performance. Sustain Energy Technol Assessments 2020;38:100681.
[49] Mozdzierz M, Berent K, Kimijima S, Szmyd JS, Brus G. A multiscale approach to the numerical simulation of the solid oxide fuel cell. Catalysts 2019;9:253.
[50] Bertei A, Ruiz-Trejo E, Tariq F, Yufit V, Atkinson A, Brandon NP. Validation of a physically-based solid oxide fuel

cell anode model combining 3D tomography and impedance spectroscopy. Int J Hydrogen Energy 2016;41:22381–93.
[51] Nenning A, Bischof C, Fleig J, Bram M, Opitz AK. The relation of microstructure, materials properties and impedance of SOFC electrodes: a case study of Ni/GDC anodes. Energies 2020;13:987.
[52] Chen Y, Zhang Y, Baker J, Majumdar P, Yang Z, Han M, et al. Hierarchically oriented macroporous anode-supported solid oxide fuel cell with thin ceria electrolyte film. ACS Appl Mater Interfaces 2014;6:5130–6.
[53] Wang F, Lyu Y, Chu D, Jin Z, Zhang G, Wang D. The electrolyte materials for SOFCs of low-intermediate temperature: review. Mater Sci Technol 2019;35:1551–62.
[54] Mogensen M, Sammes NM, Tompsett GA. Physical, chemical and electrochemical properties of pure and doped ceria. Solid State Ionics 2000;129:63–94.
[55] Jaiswal N, Tanwar K, Suman R, Kumar D, Upadhyay S, Parkash O. A brief review on ceria based solid electrolytes for solid oxide fuel cells. J Alloys Compd 2019;781:984–1005.
[56] Lübke S, Wiemhöfer HD. Electronic conductivity of Gd-doped ceria with additional Pr-doping1Dedicated to Prof. Dr. Bernt Krebs on the occasion of his 60th birthday.1. Solid State Ionics 1999;117:229–43.
[57] Inaba H, Tagawa H. Ceria-based solid electrolytes. Solid State Ionics 1996;83:1–16.
[58] Riegraf M, Costa R, Schiller G, Friedrich KA, Dierickx S, Weber A. Electrochemical impedance analysis of symmetrical Ni/Gadolinium-Doped ceria (CGO10) electrodes in electrolyte-supported solid oxide cells. J Electrochem Soc 2019;166:F865.
[59] Bischof C, Nenning A, Malleier A, Martetschläger L, Gladbach A, Schafbauer W, et al. Microstructure optimization of nickel/gadolinium-doped ceria anodes as key to significantly increasing power density of metal-supported solid oxide fuel cells. Int J Hydrogen Energy 2019;44:31475–87.
[60] Nenning A, Holzmann M, Fleig J, Opitz AK. Excellent kinetics of single-phase Gd-doped ceria fuel electrodes in solid oxide cells. Mater Adv 2021;2:5422–31.
[61] Lu X, Tjaden B, Bertei A, Li T, Li K, Brett D, et al. 3D characterization of diffusivities and its impact on mass flux and concentration overpotential in SOFC anode. J Electrochem Soc 2017;164:F188.
[62] Leonide A, Apel Y, Ivers-Tiffee E. SOFC modeling and parameter identification by means of impedance spectroscopy. ECS Trans 2009;19:81.
[63] Clematis D, Ferrari T, Bertei A, Asensio AM, Carpanese MP, Nicolella C, et al. On the stabilization and extension of the distribution of relaxation times analysis. Electrochim Acta 2021;391:138916.
[64] Sonn V, Leonide A, Ivers-Tiffée E. Combined deconvolution and CNLS fitting approach applied on the impedance response of technical Ni / 8YSZ cermet electrodes. J Electrochem Soc 2008;155:B675.
[65] Tjaden B, Brett DJL, Shearing PR. Tortuosity in electrochemical devices: a review of calculation approaches. Int Mater Rev 2018;63:47–67.
[66] Sanna C, Squizzato E, Costamagna P, Holtappels P, Glisenti A. Electrochemical study of symmetrical intermediate temperature - solid oxide fuel cells based on La0.6Sr0.4MnO3/Ce0.9Gd0.1O1.95 for operation in direct methane/air. Electrochim Acta 2022;409:139939.
[67] Riegraf M, Yurkiv V, Costa R, Schiller G, Friedrich KA. Evaluation of the effect of sulfur on the performance of nickel/gadolinium-doped ceria based solid oxide fuel cell anodes. ChemSusChem 2017;10:587–99.
[68] Grosselindemann C, Russner N, Dierickx S, Wankmüller F, Weber A. Deconvolution of gas diffusion polarization in Ni/Gadolinium-Doped ceria fuel electrodes. J Electrochem Soc 2021;168:124506.
[69] Fleig J. On the current–voltage characteristics of charge transfer reactions at mixed conducting electrodes on solid electrolytes. Phys Chem Chem Phys 2005;7:2027–37.
[70] Clematis D, Barbucci A, Presto S, Viviani M, Carpanese MP. Electrocatalytic activity of perovskite-based cathodes for solid oxide fuel cells. Int J Hydrogen Energy 2019;44:6212–22.
[71] Hirschorn B, Orazem ME, Tribollet B, Vivier V, Frateur I, Musiani M. Determination of effective capacitance and film thickness from constant-phase-element parameters. Electrochim Acta 2010;55:6218–27.
[72] François M, Carpanese MP, Heintz O, Lescure V, Clematis D, Combemale L, et al. Chemical degradation of the La0.6Sr0.4Co0.2Fe0.8O3−δ/Ce0.8Sm0.2O2−δ interface during sintering and cell operation. Energies; 2021.
[73] Adler SB. Factors governing oxygen reduction in solid oxide fuel cell cathodes. Chem Rev 2004;104:4791–844.
[74] Unachukwu ID, Vibhu V, Uecker J, Vinke IC, Eichel R-A, de Haart LGJ. Electrochemical impedance analysis and degradation behavior of a Ni-GDC fuel electrode containing single cell in direct CO2 electrolysis. J CO2 Util 2023;69:102423.
[75] Singh B, Ghosh S, Aich S, Roy B. Low temperature solid oxide electrolytes (LT-SOE): a review. J Power Sources 2017;339:103–35.
[76] Endler C, Leonide A, Weber A, Tietz F, Ivers-Tiffée E. Long-term study of MIEC cathodes for intermediate temperature solid oxide fuel cells. ECS Trans 2009;25:2381.
[77] Mo B, Rix J, Pal U, Basu S, Gopalan S. Characterizing performance of electrocatalyst nanoparticles infiltrated into Ni-YSZ cermet anodes for solid oxide fuel cells. J Electrochem Soc 2020;167:54515.